Two-Photon NAD(P)H-FLIM reveals unperturbed energy metabolism of *Ascaris suum* larvae, in contrast to host macrophages upon artemisinin derivatives exposure

Zaneta D. Musimbi[1], Arkadi Kundik[1], Jürgen Krücken[2], Anja E. Hauser[3,4], Sebastian Rausch[1], Peter H. Seeberger[5], Raluca Niesner[6,7#], Ruth Leben[1,6,7#], Susanne Hartmann[1*#]

[1] Institute of Immunology, Centre of Infection Medicine, Freie Universität Berlin, Berlin, Germany

[2] Institute for Parasitology and Tropical Veterinary Medicine, Freie Universität Berlin, Berlin, Germany

[3] Department of Rheumatology and Clinical Immunology, Charité-Universitätsmedizin Berlin, corporate member of Freie Universität Berlin and Humboldt-Universität zu Berlin, Berlin, Germany

[4] Immune Dynamics, Deutsches Rheuma-Forschungszentrum (DRFZ), a Leibniz Institute, Charitéplatz 1, Berlin, Germany

[5] Max Planck Institute of Colloids and Interfaces, Potsdam, Germany

[6] Biophysical Analytics, Deutsches Rheuma-Forschungszentrum (DRFZ), Berlin, Germany

[7] Dynamic and functional in vivo Imaging, Veterinary Medicine, Freie Universität Berlin, Berlin, Germany

***** Corresponding Author
Susanne.Hartmann@fu-berlin.de

[#]Equally contributing authors

Abstract

Two-photon microscopy combined with NAD(P)H fluorescence lifetime imaging (FLIM) provides the potential to decipher NAD(P)H-dependent energy metabolism of living cells and organisms. Soil transmitted helminths are highly prevalent with *Ascaris lumbricoides* infecting millions of people in sub-Saharan Africa and *Ascaris suum* being prevalent in pigs. The artemisinin derivatives artesunate, artemether and dihydroartemisinin (ARTs) are reported to influence energy metabolism of parasites, tumours and immune cells. Herein, two-photon NADPH-FLIM was applied to investigate the metabolism of *A. suum* third-stage larvae (L3) and porcine macrophages exposed to ARTs. Our data show *A. suum* L3 and porcine macrophages to exhibit a steady-state energy profile of high aerobic / low anaerobic glycolysis. Exposed to ARTs the macrophages decreased their general metabolic activity, without changing specific metabolic pathways. In *A. suum* larvae two-photon NAD(P)H-FLIM revealed two metabolically distinct larval regions exhibiting particularly high DUOX-like

activity in the pharynx in contrast to the midgut. The metabolic profile of both regions were, however, unperturbed by ARTs exposure. Taken together, two-photon NAD(P)H-FLIM empowered the study of specific metabolic pathways in *Ascaris* larvae as well as in host macrophages, which is particularly relevant for the mechanistic understanding of drug action on the metabolism of both parasite and host.

Introduction

Label-free NAD(P)H fluorescence lifetime imaging (FLIM) has the ability to assess the metabolic profiles of living cells and tissues at subcellular level[1] and has been applied to characterize cellular metabolism both under physiologic and pathologic conditions[2–6]. As the NAD(P)H fluorescence lifetime depends on the enzyme to which the NADH or NADPH co-enzymes bind to, the method allows for the classification of enzymatic activities involved in various energy metabolic pathways or in oxidative burst[7–9]. It has been shown that shorter NAD(P)H fluorescence lifetimes caused by increased lactate dehydrogenase (LDH, 1600 ps) activity are found in progenitor or tumor cells, with increased anaerobic glycolytic metabolism, whereas differentiated cells, with aerobic glycolytic metabolism involving oxidative phosphorylation (OxPhos), display longer NAD(P)H fluorescence lifetimes caused by increased pyruvate dehydrogenase (PDH, 2500 ps) activity[10–12]. Even longer NAD(P)H fluorescence lifetimes (3650 ps) have been shown to identify oxidative burst or oxidative stress, by activated NADPH oxidases generating reactive oxygen species[9,13]. Additionally, oxidative stress has been shown to be associated with extreme fluorescence lifetimes (7800 ps) of oxidized lipids, unrelated to NAD(P)H fluorescence[11,14].

As NAD(P)H are ubiquitous metabolic factors, NAD(P)H-FLIM can be applied to a wide range of cell types in mammals, including immune cells such as macrophages[15–17]. It has been shown that macrophages can switch their metabolism after cytokine-induced *in vitro* polarization towards a pro- or anti-inflammatory phenotype, from increased anaerobic glycolytic pathways, involving cytosolic LDH activity, to aerobic glycolytic pathways (OxPhos), involving mitochondrial PDH activity.

Since the NAD(P)H co-enzymes are partly evolutionarily conserved, the NAD(P)H-FLIM technique also allows the investigation of the metabolism of non-mammalian species, including various types of parasites. We have previously adapted and applied NAD(P)H-FLIM to study the metabolism of the murine helminth *Heligmosomoides polygyrus* and of the host intestine *in situ*[18,19]. Others have applied the method to investigate the germline of live *C. elegans* nematodes[20] or the manipulation of host cell metabolism by *Toxoplasma gondii*[21]. Thus, NAD(P)H-FLIM represents a unique tool to analyze cellular metabolism across species, with particular relevance for our understanding of parasitism.

Soil transmitted helminths infect approximately one billion people worldwide[22], *Ascaris lumbricoides* being highly prevalent in sub-Saharan Africa[23]. Infection with the roundworm *A. lumbricoides* is associated with significant morbidity[24–26], hence ascariosis is a major public health concern in the affected countries. *Ascaris lumbricoides* is capable of interbreeding with the pig roundworm and thereby forms a genetic complex with *A. suum* [27], which is highly prevalent in pig-farming, resulting in high economic losses[28]. The *Ascaris* life cycle involves four stages: third-stage larvae (L3) hatch from ingested embryonated eggs within the small intestine, followed by larval migration through the caecum and liver to the lungs. During the migration the larvae are under constant attack of immune cells with macrophages being an important immune cell fighting the migrating worm larvae. Whilst monocyte derived macrophages are reported to immobilize *Ascaris* larvae *in vitro* [29], migratory larvae activated alveolar and interstitial macrophage activity in the lung of the mouse model[30]. Once matured, L3 penetrate the alveolar migrate to the trachea, are coughed up and swallowed back to the small intestine. In the small intestines, L3 molt molt to fourth-stage larvae (L4) and complete the life cycle after a final molt as adults[31]. During the hepato-tracheal migration, the larvae are reported to utilize aerobic respiration which is not only necessary for their development but also due to the host oxygen enriched environment [32,33]. Within the intestines metabolism is switched towards anaerobic respiration[34,35], with a partially reversed tricarboxylic acid cycle (TCA) cycle and high malate dehydrogenase (MDH) activity.

Artemisinin and its semi-synthetic derivatives, dihydroartemisinin, artesunate, arteether and artemether (ARTs), are endoperoxide sesquiterpene lactones majorly known for their antimalarial activity[36]. In addition to antimalarial properties, ARTs are pharmacologically active against other protozoan and helminth parasites, viruses, and cancers[37]. Their mode of action is reported to be through heme adduct formation, protein alkylation, free radical production[38] and, most recently, interference with palmitoylation[39]. Energy metabolic pathways have also been implicated as both direct and indirect targets of ARTs[40–46]. Due to the reported anthelmintic activity and possible metabolic influence, the current study used ARTs as a drug model with a potential to influence the energy metabolism of porcine alveolar-derived macrophages and *A. suum* L3.

Herein, we adapted and applied two-photon microscopy combined with NAD(P)H fluorescence lifetime imaging (FLIM) to investigate NAD(P)H-dependent enzymatic activities involved in energy production and oxidative burst (defense metabolism) of both the parasitic nematode *A. suum* L3 and a porcine alveolar-derived macrophage cell line. Further, the method was used to assess the impact of ARTs on the larval and macrophage general metabolic activity and specific enzymatic activity, related to energetic metabolic pathways or oxidative burst. At steady state, both *A. suum* L3 and porcine macrophages adopt a metabolic profile of high OxPhos and low anaerobic glycolysis. In *A.*

suum L3, we found two metabolically distinguishable larval regions; with the pharynx exhibiting DUOX-like enzyme activity. Exposure to ARTs altered the general metabolic activity of the porcine macrophages but not their preferential enzymatic activity, with no influence on the metabolism of *A. suum* L3.

Materials and Methods

Drugs and chemicals

Artemisinin (purified as per Zhou *et al.*[47]), artemether (CAS RN 71963-77-4) and artesunate (CAS RN88495-63-0) were provided by the Seeberger laboratory at Max Planck Institute of Colloids and Interfaces (Potsdam, Germany). Drug stock solutions of 100 mM were prepared in 100% DMSO and stored at -20°C.

Ascaris suum egg collection, embryonation and hatching

Ascaris suum eggs were collected from *A. suum* female adults obtained from a slaughterhouse, prepared and cultured[48]. Briefly, the female adults were separated from males and washed with 0.9% physiological NaCl. Thereafter, they were incubated for three days in balanced salt solution (HBSS-AB: 127 mM NaCl, 7.5 mM NaHCO3, 5 mM KCl, 1 mM CaCl2, 1 mM MgCl2), 0.1% glucose, 200 U/ml penicillin, 200 µg/ml streptomycin, 2.5 µg/ml amphotericin and 50 µg/ml gentamycin (PAN-Biotech GmbH, Germany) (referred to as medium hereafter) at an atmosphere of 37 °C, 5% CO_2. *Ascaris suum* eggs were collected every 24 hours whilst changing the media. The harvested eggs were washed and incubated at 30 °C for embryonation. Fully embryonated eggs were washed and separated from un-fertilized and un-embryonated eggs using a sucrose step gradient of 18, 20 and 23% (w/v)[49]. Embryonated *A. suum* eggs (recovered from 23% sucrose layer) were then hatched using the glass bead method[50] with slight modifications. Briefly, eggs in medium were added into an Erlenmeyer flask containing glass beads and hatching occured in an incubator shaker at 37 °C, 100 rpm. To separate the hatched *A. suum* larvae from eggshells or unhatched larvae, content in the Erlenmeyer flask was washed, transferred onto a 30 µM sieve in 100 ml beaker containing 10 ml HBSS media and incubated at 37 °C, 5% CO_2 for a minimum of three hours and a maximum of 15 hours to allow for migration. Migrated larvae were washed and immediately used for drug exposures.

In 96 well plates, *A. suum* (~1000 L3/well) in media were exposed to artesunate and artemether at concentrations of 20- and 200 µM for 24 hours at 37 °C and 5% CO_2 with vehicle and negative controls run in parallel. Worms were washed three times with fresh medium and transferred into 1.5 ml microcentrifugation tubes. Worms were transferred to glass slides and immobilized by NemaGel

(In Vivo Biosystems, Eugene, Oregon, USA). NemaGel was used to trap the worms for imaging without injuring them.

Porcine alveolar-derived macrophages

Porcine alveolar-derived macrophages (PAM 3D4/31) were cultured in complete Iscove's Modified Dulbecco's Medium (IMDM (PAN-Biotech GmbH, Germany) supplemented with 10% heat-inactivated fetal calf serum, 1% penicillin/streptomycin; herein referred to as CIMDM). The cultures were maintained at 37 °C and 5% CO_2. In 6 well plates, the porcine macrophages (2×10^6 cells/well) were seeded overnight and exposed to artesunate at 0.1- and 1 µM for 24 hours at 37 °C and 5% CO_2 with vehicle and negative controls run in parallel. Experiments were done in duplicate. For imaging, CIMDM was aspirated and replaced with 2 ml DPBS.

Two-photon microscopy FLIM

The two-photon FLIM experiments were carried out on a specialized commercial laser scanning microscope (TriMScope II, LaVision Biotec, Miltenyi, Bielefeld, Germany), as previously described[8] with a Titanium: Sapphire laser (80 MHz, 140 fs pulses, Chameleon Ultra II, Coherent, Duisburg, Germany) tuned at 765 nm for NAD(P)H excitation. The beam was focused into the sample by a water-immersion objective (20×, NA 1.05, Apochromat, Olympus, Hamburg Germany). NAD(P)H fluorescence was collected in the range 466±30 nm by a GaAsP PMT (Hamamatsu, Herrsching, Germany) connected to a time-correlated single photon counting device (TCSPC LaVision Biotec, Miltenyi, Bielefeld, Germany) with 55 ps bin width, over at least 9 ns. The acquired images were typically 200x200 µm² for the macrophages and 245 × 245 µm for the larvae (both at 512 × 512 pixels), the pixel dwell time was 5.877 s. Five fields of view (FoV) were imaged in fast mode per sample to increase pixel dwell time and thus the signal-to-noise ratio. The photon arrival histograms were subsequently added up before analyzing.

NAD(P)H- dependent enzymes used for the phasor analysis of NAD(P)H-FLIM data

Transcriptome analysis of mammalian cells was used to obtain thirteen most abundant NAD(P)H-dependent enzymes as detailed in Table 1. These were used for the phasor analyses of the porcine macrophages data (see next paragraph). Before this analytical system was applied to *A. suum*, the expression of these enzymes in *A. suum* was verified using the genome database for parasitic worms "WormBase ParaSite" (https://parasite.wormbase.org/index.html, last view 16.08.2023; original source of the *Ascaris* data set[51]) and the proteins confirmed via mass spectrometry of *A. suum* L3. The protein sequences were obtained from the UniProt database[52] and blasted against the respective human enzymes. The InterPro database[53] was thereafter used to determine the homology of the

NAD(P)H binding sites. The system was adapted accordingly (Table 1). Since no DUOX enzyme was annotated in the *A. suum* genome, the human DUOX enzyme sequence was blasted against *A. suum* genome. The resulting unannotated sequence was blasted against *Caenorhabditis elegans*, and homology of NAD(P)H determined. It was further referred to as DUOX-like enzyme in the text.

Table 1. Abundant NAD(P)H-dependent enzymes present in mammalian cells and *A. suum* L3

Abbreviation	**Full name**	**Fluorescence lifetime of NAD(P)H [ps]**	**Mammalian cell pathways involved**	**Expression in *A. suum* L3**
nan	pixel could not be allocated	-	-	-
Free NAD(P)H	Unbound NAD(P)H	450	Inactive metabolism	✓
MDH	Malate dehydrogenase	1240	TCA cycle	✓
HADH	Hydroxy acyl-coenzyme-A dehydrogenase	1360	Beta oxidation	✓
LDH	Lactate dehydrogenase	1600	Anaerobic glycolysis/ fermentation	✓
G6PDH	Glucose-6-phosphate dehydrogenase	2005	Pentose phosphate pathway	x
SDH (NADH)	Sorbitol dehydrogenase (bound to NADH)	2010	Fructose synthesis	x
GAPDH	Glyceraldehyde-3-phosphate dehydrogenase	2050	Glycolysis	✓
IDH	Isocitrate dehydrogenase	2170	TCA cycle	✓
SDH (NADPH)	Sorbitol dehydrogenase (bound to NADPH)	2260	Fructose synthesis	x
PDH / CTBP1	Pyruvate dehydrogenase / C-terminal binding protein 1 (nuclear)	2470	Acetyl-CoA synthesis/gene silencing	✓ (PDH) x (CTBP1))
iNOS	Inducible nitric oxide synthase	2550	Immune defense	x
ADH	Alcohol dehydrogenase	2600	Detoxification	✓
NOX/DUOX	Activated NADPH oxidation	3650	Oxidative burst	✓ DUOX x NOX
	✓ “is expressed”; x “is not expressed”			

The time-domain fluorescence lifetime data were analyzed by an algorithm written in Python (Version 3.9.7)[8]. In brief, the add-up photon arrival histogram was transformed into the normalized phase domain by computing the discrete Fourier transformation, resulting in a complex number consisting of a real and imaginary part which give the coordinates in a phasor plot[54] (Supplementary Fig. S1). The half circle in the normalized phasor plot represents all possible mono-exponential fluorescence lifetimes and limits the range that can be used for analysis. By adequate signal-to-noise ratio (SNR > 5)[55] each pixel in the phasor plot was assigned to one of the ten most abundant NAD(P)H-dependent enzymes found in *A. suum*.

After assigning each pixel in the images to one of the NAD(P)H-dependent enzymes or unbound NAD(P)H, these pixels were transferred back to space domain to create an enzyme map (Supplementary Fig. S1). In the phasor plot, the length of the vector pointing from free/unbound NAD(P)H "free" towards the position of the lifetime of the assigned enzyme gives the enzyme-bound NAD(P)H activity in each pixel of the image (Supplementary Fig. S1). Pixels with a fluorescence lifetime of 0.45 ns indicate unbound NAD(P)H and are interpreted to have a metabolically inactive status, since no NAD(P)H-dependent metabolic process is catalyzed. Enzymes dominant in anaerobic glycolysis/ β-oxidation of fatty acids are described to have shorter fluorescence lifetimes ranging between 1-2.26 ns whilst enzymes dominant within aerobic glycolysis/oxidative phosphorylation (OxPhos) are described to have longer fluorescence lifetimes ranging between 2.47-2.6 ns. Therefore, pixels with fluorescence lifetimes of 1.24 – 2.6 ns are collectively classified as being active in energy metabolism. NAD(P)H bound to NADPH oxidases have been described as having a very long fluorescence lifetime of 3.65 ns[56].

Segmentation

Ascaris suum larvae

At first glance, the images of *A. suum* larvae showed two regions with different NAD(P)H FLIM properties. The NAD(P)H fluorescence intensity of the larvae within the posterior region was brighter compared to that of the anterior region (Supplementary Fig. S1a, first column). The fluorescence lifetime images with false color representation indicated varying NAD(P)H lifetimes within the larvae (Supplementary Fig. S1a, second column). The anterior region that was inclusive of the internal and external section of the larvae, were referred to as pharynx, and posterior region more internal to the body, were referred to as midgut [57] (Supplementary Fig. S1a, third column). Lifetimes were allocated to binding of the co-enzyme to its respective partners in the phase domain, with enzyme vectors pointing from unbound "free" NAD(P)H to enzyme-bound NAD(P)H, as depicted by the phasor plot (Supplementary Fig. S1b). The allocated enzymes and enzyme vector lengths were assigned respective colors (color key scale with respective enzyme names and percentage activity on the right of Supplementary Fig. S1b) allowing for the visualization of the enzyme and activity map, respectively, within the larval regions.

In order to analyze the two regions systematically, we separated the *A. suum* images in these two regions by performing image segmentation using the fast random forest-based pixel classification algorithm LABKIT (Fiji plugin, https://imagej.net/plugins/labkit/ downloaded 16th March 2023)[58]. The algorithm was trained by manually identifying the pharynx, midgut, and background regions in some of the NAD(P)H intensity images, afterwards the trained algorithm was applied to the remaining

images. In each FoV, the segmentation resulted in two binary masks for the two annotated image regions. We multiplied both the enzyme and activity maps of each FoV by the corresponding binary masks for the regions 1 and 2 (Supplementary Fig. S1c and S1d). The activity gives the ratio of enzyme-bound NAD(P)H to total NAD(P)H: 0% indicating metabolic inactivity (only free NAD(P)H) to 100% indicating highly active, complete binding to the enzymes. The percentual enzyme-bound NAD(P)H activity is represented in maps (Supplementary Fig. S1d). To quantify the findings, we averaged the NAD(P)H-dependent enzymatic activity to a mean value per body region and larva and plotted them. Since the enzyme allocation is not continuous like the activity maps but discrete, we present the histograms of the enzyme maps to analyze its diversity.

Porcine macrophages

Each NAD(P)H-FLIM image of the porcine macrophages contained approximately 150-200 cells. To display the heterogeneity of the single cells, we segmented two fields of view of each treatment for the single cells with LABKIT, obtaining approximately 300-400 cells per treatment. We applied the resulting masks to the corresponding enzyme and activity maps. To quantify the findings, we averaged the NAD(P)H-dependent enzymatic activity to a mean value per cell and plotted them. Furthermore, for the macrophages we grouped enzymes with similar NADH(P)H fluorescence lifetimes: LDH-like (1.24 ns – 2.005 ns), PDH-like (2.17 ns – 2.60 ns) and NOX (3.65 ns), and calculated the proportion of the pixel area of the assigned enzyme group in the pixel area of the segmented cell (fraction/cell area).

Data analysis

As all drugs were dissolved in DMSO, data analysis was done in comparison to the DMSO vehicle control. To quantify the NAD(P)H-FLIM results, anterior/ posterior segmentation was applied to both enzyme maps and free: enzyme-bound NAD(P)H “activity” maps. The segmented activity maps were averaged over the entire respected body region, resulting in a mean free: enzyme-bound NAD(P)H “activity” value for every larva for each anterior and posterior region; at least ten larvae were imaged per treatment. To analyze the enzyme maps their histograms were generated for anterior and posterior region of the larvae and normalized for the pixel area resulting in fraction of the respected enzyme per area. The normalized enzyme histograms as well as the mean value free: enzyme-bound NAD(P)H “activity” were used as features in supervised uniform manifold approximation and projection (UMAP) with k nearest neighbor (KNN) clustering and unsupervised principal component analysis (PCA) with k-means clustering for dimension reduction and analysis. To quantify the macrophage NAD(P)H-FLIM results, the grouped enzymes and activity maps were averaged over the whole FoV resulting in a mean value for each FoV (ten images per treatment).

Results

High OxPhos/low anaerobic glycolysis metabolic profile of porcine alveolar-derived macrophage cell line

Macrophage cell lines are highly characterized by their proliferation and immortalization which, inarguably, can lead to modification in energy metabolism when compared to their primary counterparts. Macrophages used were of cell line descent hence their steady-state metabolic profile was initially determined by analyzing data from cells in the medium group. The fluorescence intensity of the macrophages (Fig. 1a, first column) and fluorescence lifetime images with false color representation indicating NAD(P)H lifetimes within the macrophages (Fig. 1a, second column) were determined and analyzed by our phasor approach (Fig. 1a, third column). The allocated enzymes and enzyme vector lengths were assigned respective colors (color key scale with respective enzyme abbreviation and percentage activity at the bottom of Fig. 1a, fourth and fifth column) allowing for the visualization of the enzyme and activity map, respectively.

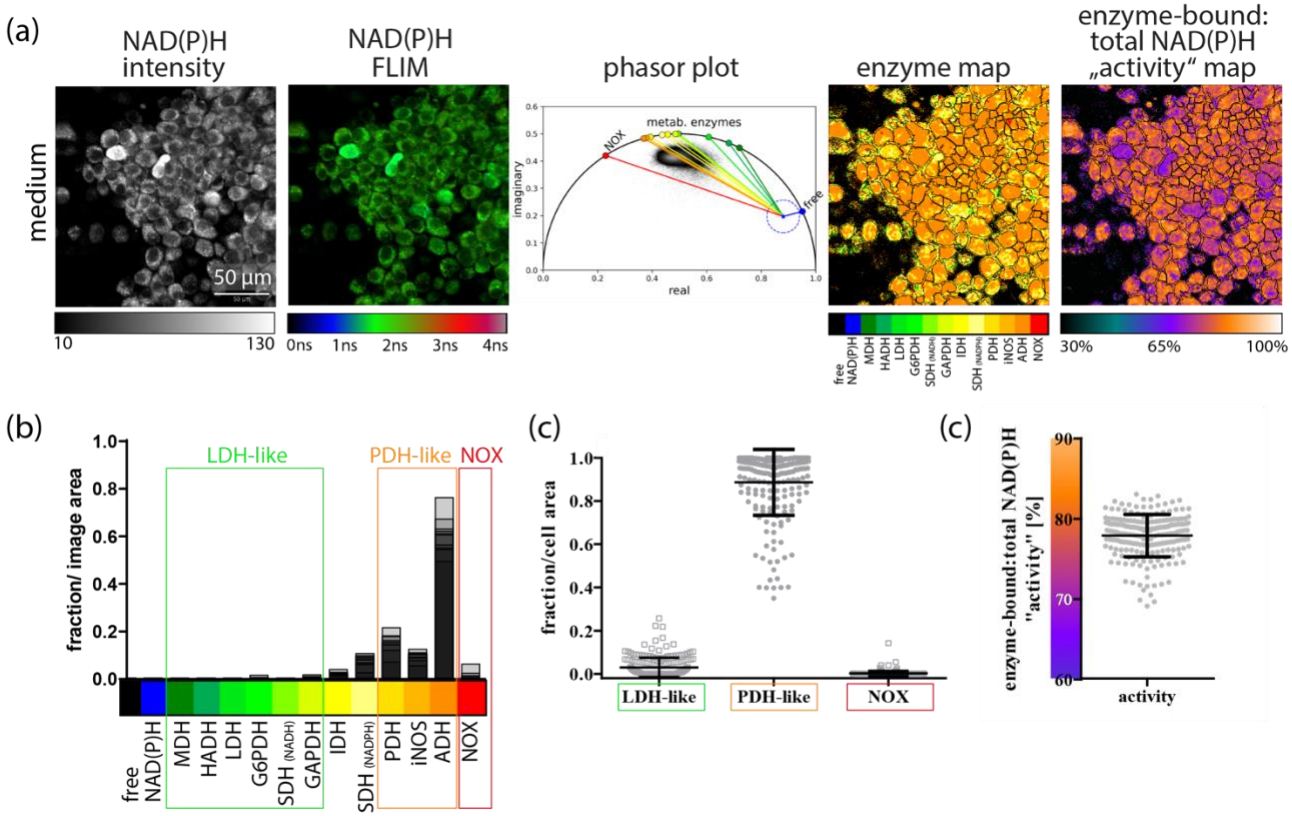

Fig.1 Metabolic profile of the porcine alveolar-derived macrophage cell line. (a) Representative microscopic image (one from ten). From left to right: NAD(P)H fluorescence intensity – the scale bar indicates 50 µm and applies for all shown images; NAD(P)H fluorescence lifetime image in false colour representation ranging from 0 – 4 ns; corresponding phasor plot with enzyme vectors pointing from unbound "free" NAD(P)H to NAD(P)H bound to various enzymes, map of the allocated NAD(P)H-dependent enzymes; map of the enzyme-bound: total NAD(P)H activity in false colour representation ranging from 30 – 100%. **(b)** Superimposed enzyme histograms of ten FoVs, each averaged over the entire FoV with "LDH-like", "PDH-like" and "NOX" groupings. **(c)** Plotted proportion of the pixel area of the assigned enzyme group in the pixel area (fraction/cell area) of the segmented

cells. **(d)** Averaged enzyme-bound: total NAD(P)H activity of the segmented cells. (c & d) Each gray dot represents a single cell.

A metabolic state of inactivity was denoted by free NAD(P)H. An active energy production metabolic state was considered when NAD(P)H was bound to the enzymes MDH, HADH, LDH, GAPDH, IDH, PDH, ADH, whilst active oxidative burst was implied when NAD(P)H was bound to NOX enzyme. Based on the similarity of the NAD(P)H fluorescence lifetimes (see Table 1) MDH, HADH, LDH, GAPDH enzymes were grouped into LDH-like enzymes and IDH, PDH, ADH were grouped into PDH-like enzymes denoting anaerobic glycolysis and OxPhos respectively (Fig. 2b). Analysis of the cells in medium revealed an energy metabolic profile of high aerobic i.e. OxPhos/low anaerobe glycolysis as depicted by the high composition of PDH-like enzymes and low composition of LDH-like enzymes (Fig. 1c). Also observed was the low composition of enzymes involved in oxidative burst (NOX). At steady state, the macrophages were observed to have an enzyme activity of ~77% (Fig. 1d).

NAD(P)H-FLIM reveals a decrease in metabolic activity in macrophages exposed to artesunate

We employed two-photon NAD(P)H-FLIM to determine drug induced metabolic alterations in porcine macrophages, i.e. important immune cells of the host. Porcine alveolar-derived macrophage cell line was exposed to 0.1 and 1 µM artesunate for 24 hours. Via two-photon NAD(P)H-FLIM approach we analyzed enzyme activity and overall metabolic activity of ART-exposed macrophages (Fig. 2a). The analysis of the porcine macrophages in medium, both of single segmented cells (grey dots in Fig. 2b) and in bulk, over the entire field of view (FoV) (black dots in Fig. 2b), compared to DMSO showed an unchanged overall metabolic activity (~77%) (Fig. 2b) (Supplementary Fig. S2). However, the grouping of enzymes revealed that the proportion of pixels assigned to the PDH-like group decreased significantly after exposure to DMSO, while the LDH-like group likewise increased. This indicated that the macrophages slightly balance their energy household toward anaerobic glycolysis (LDH activity) since the oxygen availability may be decreased by DMSO oxidation. Next, the enzyme and activity maps of macrophages exposed to artesunate were investigated (Fig. 2b). In comparison to macrophages exposed to DMSO, the NAD(P)H dependent overall metabolic activity of macrophages exposed to artesunate (1 µM) significantly decreased (73.24%; $p \leq 0.001$). The analysis of single segmented cells (grey dots) demonstrated the metabolic diversity of cells within one FoV, concerning both the preferential enzymatic activity and the general metabolic activity.

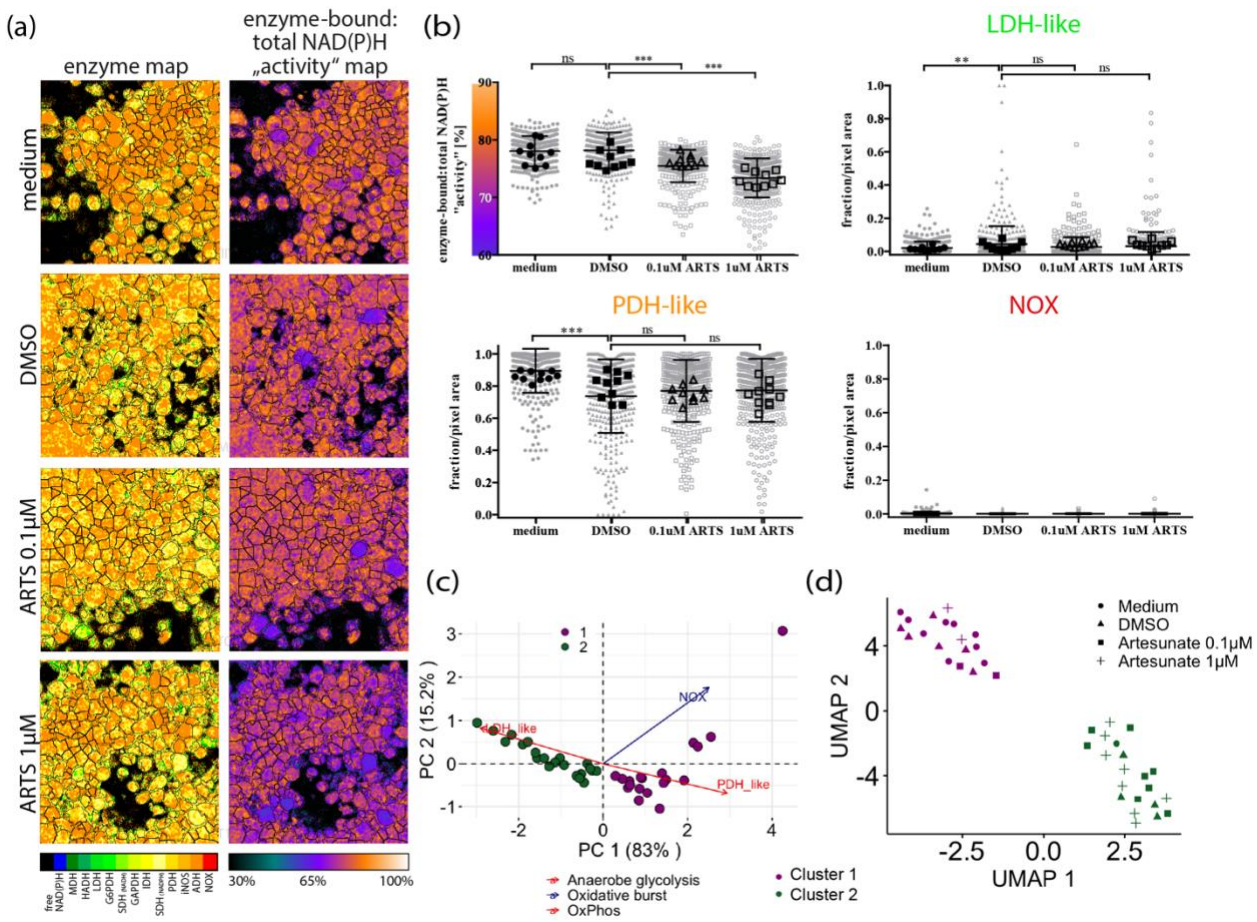

Fig. 2. Artesunate alters the metabolic activity of macrophages. Porcine macrophages were exposed to 0.1- and 1 µM of artesunate (ARTS) for 24 hours and evaluated using two-photon NAD(P)H-FLIM. **a**) Representative microscopic image of macrophages. Left: map of the allocated NAD(P)H-dependent enzymes; right: map of the enzyme-bound: total NAD(P)H activity in false colour representation ranging from 30 – 100%. (**b**) Plots for quantification. Upper left: Averaged enzyme-bound: total NAD(P)H activity of the segmented cells of two FoVs(grey symbols each representing a single cell) superimposed with averaged enzyme-bound: total NAD(P)H activity of the entire image (ten per treatment, black symbols); Rest: Plotted fraction of the pixel area of the assigned respected enzyme group in the pixel area of the entire segmented cells (grey symbols) or the entire image (ten per treatment, black symbols). The statistics refer to the segmented cells. Significance is represented by $p < 0.0001$: ****; $p \leq 0.001$: ***; $p \leq 0.01$: ** ; $p \leq 0.05$: * ; $p \geq 0.05$: ns; Kruskal-Wallis test with Dunn's post-hoc. The PCA biplot of ten FoVs per condition **(c)** represents the association between the clusters and the grouped enzymes within PC1 and PC2. Cluster 1 and 2 are represented by purple and green dots respectively whilst enzymes associated with energy production and oxidative burst are depicted in red and blue arrows and texts respectively. The UMAP plot **(d)** illustrates ART exposures within clusters. Cells exposed to artesunate at concentrations of 0.1- and 1 µM, DMSO and medium are represented by a square, plus sign, triangle and dot respectively.-FoV: Field of view.

PCA combined with K-means unsupervised clustering of the bulk FoV dataset revealed two clearly separated clusters of FoVs associated with either LDH-like and PDH-like enzymes (Fig. 2c and 2d). Enzymes associated with OxPhos (PDH-like enzymes) highly correlated with cluster 1 which mainly represented macrophages from the medium control. In contrast, cluster 2 was associated with the activity of enzymes involved in anaerobic glycolysis (LDH-like enzymes) and mainly comprised macrophages exposed to DMSO or co-exposed to artesunate and DMSO (Fig. 2c and 2d). Independent of the culture conditions, NOX activity was low and only seen in few macrophages, indicating negligible oxidative burst activity.

Collectively, macrophages have a steady state energy profile characterized by high OxPhos/low anaerobic glycolysis that is influenced by exposure to DMSO, but not by artesunate. In contrast, their overall metabolic activity is significantly decreased by exposure to artesunate.

Distinct metabolic profiles within anatomic regions of *A. suum* L3

Next, we applied NAD(P)H-FLIM to study the metabolism of *A. suum* L3 and determined two distinct metabolic profiles that were anatomically separated (Fig 3a). We observed a sharp distinction in the bound fluorescence lifetime and fluorescence intensity within the pharynx and midgut regions of the larvae (for *Ascaris* L3 anatomy see Supplementary Fig. S1a). Analysis of the enzyme activity and overall metabolic activity maps of larvae from the control condition (medium with DMSO) revealed a significantly higher ($p<0.0001$) NAD(P)H dependent overall activity in the pharynx region (72 ± 3%) compared to the midgut region of the larvae (58 ± 5%) (Fig. 3b) with a large effect size r of 0.817. Additionally, the preferential NAD(P)H-dependent enzymatic activity distribution within these two regions of the *A. suum* larvae differed (Fig. 3c). The midgut, although showing less overall activity, had high fractions of bound GAPDH, IDH, PDH, i.e., enzymes involved in the aerobic glycolytic metabolism and in OxPhos. This contrasted with the profile determined in the pharynx region, which was dominated by DUOX-like enzyme activity (Fig. 3c). Further, K-nearest neighbor (KNN) supervised analysis of the data revealed a distinct spatial segmentation between the pharynx and the midgut regions, reflecting the observed difference in enzyme activity distribution and in overall metabolic activity (Fig. 3d).

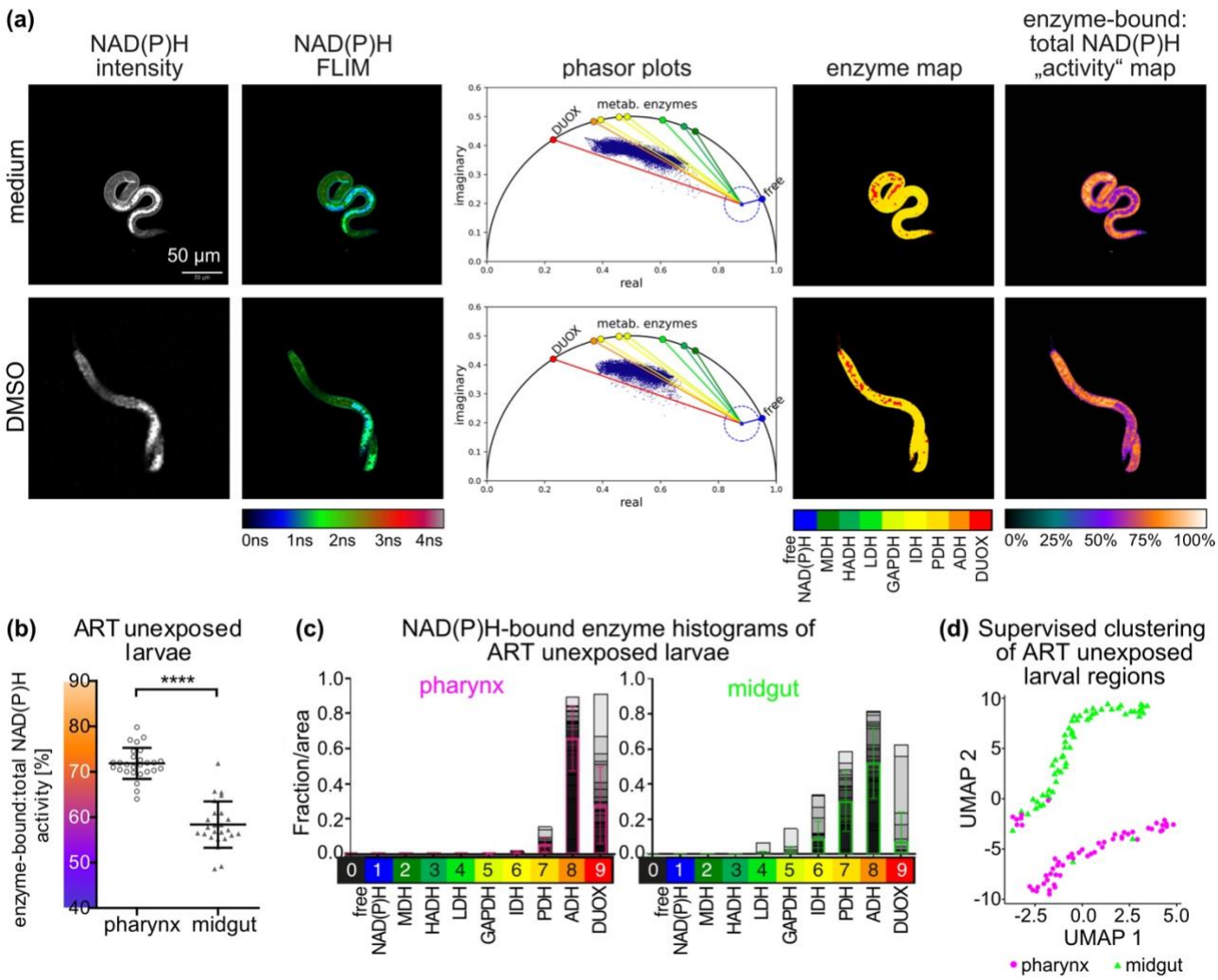

Fig. 3. Spatially distinguishable NAD(P)H-dependent metabolic fingerprints in *A. suum* L3. A representative microscopic image of L3 **(a)** visually illustrating the NAD(P)H intensities, NAD(P)H-FLIM, phasor plots, enzyme maps and activity maps in ART unexposed larvae. The scatterplot **(b)** denotes NAD(P)H enzyme activity (%) with standard deviation within the pharynx (circles) and midgut (triangles) regions of larvae unexposed to ARTs. Activity was calculated as the ratio of enzyme bound NAD(P)H to total NAD(P)H; 0% indicating enzyme inactivity (only free NAD(P)H) to 100% indicating highly active, NAD(P)H completely bound to the enzymes). The plots **(c)** denote enzyme histograms normalized to pixel area for pharynx and midgut; grey to black show the overlapped histograms of all larvae, the magenta (pharynx) and green (midgut) bars show the average over all images with standard deviation. UMAP plot **(d)** illustrates the spatial distribution of the allocated bound enzymes and the enzyme-bound: total activity within the pharynx and midgut (represented by magenta dots and green triangles respectively) of ART unexposed larvae. Scale bar indicates 50 µm and applies for all shown images. Significance is represented by $p<0.0001$: ****; Wilcoxon test.

Unperturbed metabolic profiles of pharynx and midgut regions of *A. suum* L3 upon exposure to ARTs

The viability of the ART-exposed larvae was investigated using the resazurin reduction assay and ATP bioluminescence assay. The capacity of the resazurin reduction assay to detect the metabolic activity of *Ascaris* larvae was assessed previously[49]. Only high concentrations of ARTs decreased the viability of the larvae after 48 hours of exposure. Due to the more potent effects of artemether on the general metabolic activity (Supplementary Fig. S3) and artesunate on ATP levels (Supplementary

Fig. 4), investigations in FLIM focused on exposures of the larvae to artesunate and artemether only. Larvae were exposed to 20 and 200 µM artesunate and artemether for 24 hours.

To see whether exposure to ARTs affected the NAD(P)H-dependent overall metabolic activity within the pharynx and midgut, the two-photon NAD(P)H-FLIM approach was then used to analyze enzyme activity and overall metabolic activity of ART-exposed larvae (Fig. 4a). The overall metabolic activity of ART-exposed larvae was comparable to that of the DMSO controls (Fig. 4b). K-means unsupervised and KNN supervised clustering was applied on PCA transformed data to detect the respective metabolic profiles of the *A. suum* pharynx and midgut, associated with specific enzymatic activity. We found only few larvae performing mainly oxidative burst, associated with a high contribution of DUOX-like enzymatic activity, most of them mainly displaying activity of enzymes involved in energy metabolism (Fig. 4c).

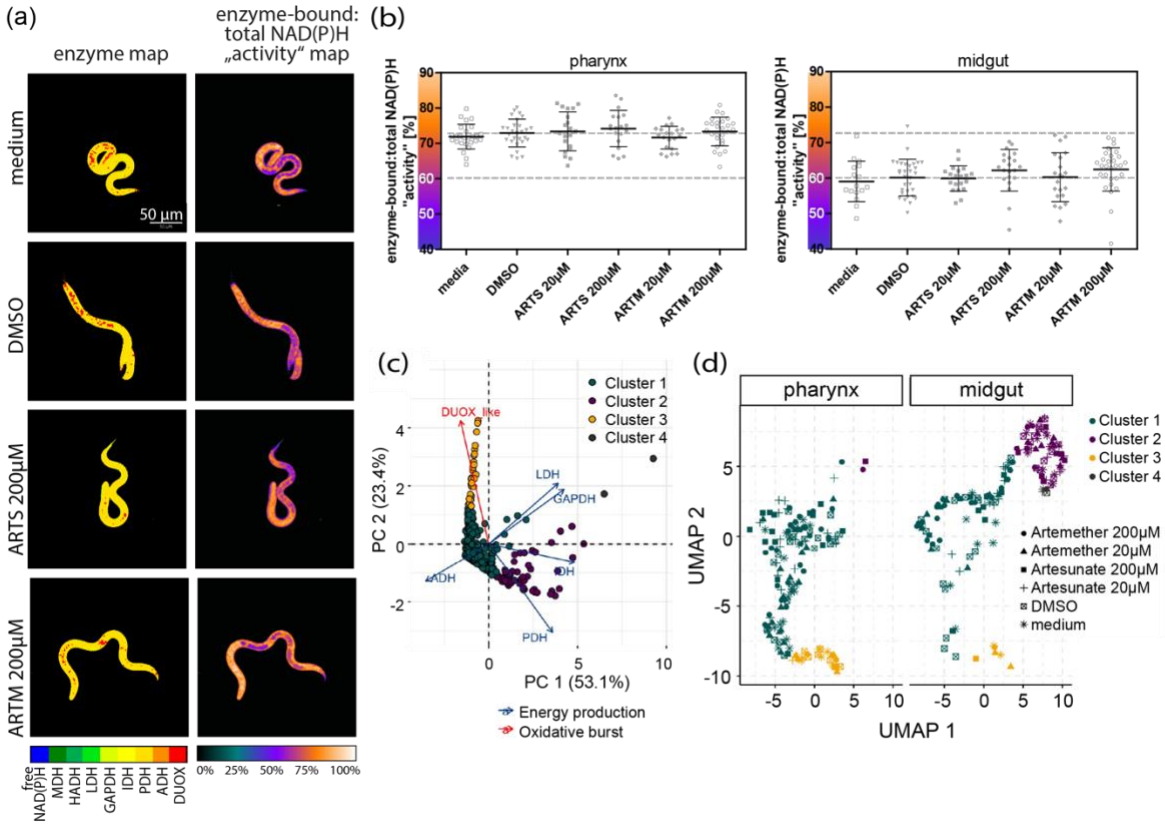

Fig. 4. Un-perturbed NAD(P)H-dependent metabolism in ARTs-exposed *A. suum* L3. *A. suum* L3 were exposed to 20- and 200 µM of artesunate (ARTS) and artemether (ARTM) for 24 hours and evaluated using two-photon NAD(P)H-FLIM. A representative microscopic image of L3 **(a)** visually illustrating the NAD(P)H enzyme map and activity map in ART exposed larvae. Dot plots of enzyme activity within the pharynx and midgut **(b)**. Activity is calculated as the ratio of enzyme bound NAD(P)H to total NAD(P)H; 0% indicating enzyme inactivity (only free NAD(P)H) to 100% indicating highly active, NAD(P)H completely bound to the enzymes). Data dimension reduction was done using PCA and transformed data used for downstream analysis. The PCA biplot **(c)** represents the association between the clusters and the bound enzymes within PC1 and PC2. Cluster one, two, three and four are represented by green, purple, yellow, and grey dots respectively whilst enzymes associated with energy production and oxidative burst are depicted in blue and red arrows and texts respectively. The UMAP plot **(d)** illustrates ART exposures within clusters grouped per region. Larvae exposed to artemether and artesunate at concentrations of 200- and 20 µM, DMSO and medium are represented by a dot, triangle, square, plus sign, an x

marked square and a star respectively. n Artesunate 200/20 µM = 38/40; n Artemether 200/20 µM = 58/40; n medium/DMSO controls = 52/60.

Energy production of the larvae was associated with a metabolic profile marked by high OxPhos-like pathways as indicated by the combined high contributions of mitochondrial enzymes PDH and IDH accompanied by low anaerobe glycolysis-like pathways, as indicated by the low contributions of the cytosolic enzyme LDH, as well as by the absence of MDH (Fig. 4c and Supplementary Fig. S5a). Upon determination of the optimal number of clusters using the silhouette method (Supplementary Fig. S5b), K-means unsupervised clustering allowed grouping the larvae into four metabolically distinct clusters. Enzyme activities associated with energy production highly correlated with clusters 1, 2 and 4, whereas DUOX-like enzyme activity associated with oxidative burst highly correlated with clusters 1 and 3 (Fig. 4c).

KNN supervised clustering was used to visualize the spatial distribution of the clusters and drug exposures within the pharynx and midgut of the PCA-transformed dataset Both the pharynx and midgut were found to preferentially use aerobic glycolysis/OxPhos for energy production, depicted by high activity of the mitochondrial enzymes PDH and IDH. However, in the pharynx we found a higher preference for DUOX-like enzyme activity associated with oxidative burst (cluster 1 and 3) as compared to the midgut (clusters 1 and 2) (Fig. 4d and Supplementary Fig. S5b). Though metabolism within the two regions differed, exposure to ARTs did not induce any metabolic profile shift in the larvae, as illustrated by the heterogenous scatter of NAD(P)H-bound enzyme activities in the pharynx and midgut regions, in both ART-exposed and unexposed larvae (Fig. 4d).

As summarized in Fig. 5, the midgut section of *A. suum* larvae was observed to have a higher activity of NAD(P)H-bound mitochondrial enzymes associated with energy metabolism, indicating a high OxPhos (high PDH and IDH) and low anaerobe glycolysis (low LDH, absence of MDH) activity. The pharynx region of the larvae had a higher contribution of DUOX-like enzyme activity. Porcine macrophages were also observed to have a high OxPhos/low anaerobe glycolysis energy metabolism at steady state (Fig. 5). Although ARTs are observed to have an influence on the NAD(P)H-dependent metabolism of host macrophages, exposure to ARTs had no impact on the NAD(P)H-dependent metabolism of the *Ascaris* larvae.

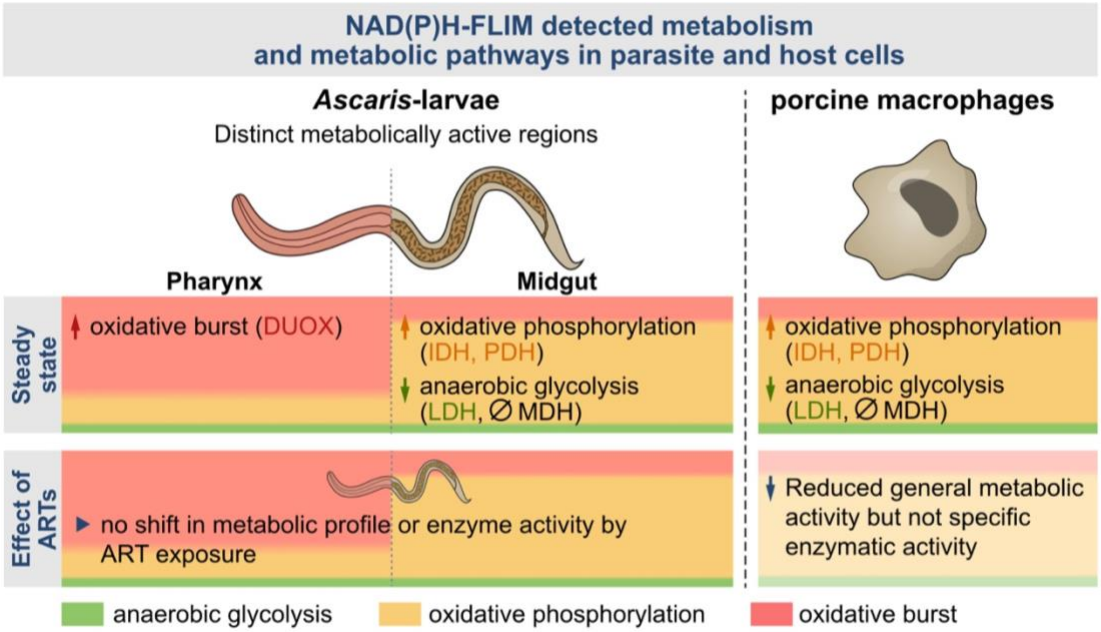

Fig. 5. Steady state energy metabolism of high OxPhos / low anaerobe glycolysis in both *Ascaris* larvae and porcine macrophages. NAD(P)H FLIM detected distinct metabolically active regions in the *A. suum* L3. Although both regions were seen to have steady state energy metabolic profiles of high OxPhos (orange) / low anaerobe glycolysis (green), the anterior region referred to as pharynx was highly associated with oxidative burst (pink) when compared to the posterior region referred to as midgut. Similarly, the porcine macrophages had a steady state energy metabolic profile of high OxPhos / low anaerobe glycolysis. Oxidative burst via NOX was however non-existent. Unlike *A. suum* L3, exposure to ARTs decreased the metabolic activity of porcine macrophages. Nonetheless, exposure to ARTs had no specific enzyme activity in both *A. suum* L3 and porcine macrophages thereby resulting in no shift in their respective steady state metabolic profiles.

Discussion

Over the past decades, fluorescence lifetime imaging (FLIM) has been successfully used to investigate the metabolism of live cells and tissues upon drug exposure, helping us to better understand drug delivery, mode of action and response[6]. NADH and NADPH are endogenously fluorescent enzyme cofactors with overlapping emission spectra, thereby being termed as NAD(P)H. Both are essential cofactors in catabolic and anabolic enzymatic reactions, thus, NAD(P)H-binding reports catalytically active enzymes. Metabolism under physiologic conditions can be studied using NAD(P)H-FLIM due to its competency to simultaneously inform on the real-time metabolic state of living cells and tissues on a subcellular level[4,5]. Here, two-photon NAD(P)H-FLIM was adapted and used to determine the metabolic profiles of porcine macrophages and *A. suum* L3 larvae. The method was used to monitor drug-induced metabolic interference in both the host cells and the parasite upon exposure to ARTs.

Cell lines are developed to allow for rapid proliferation and immortalization thereby potentially interfering with the metabolism of the primary cell. The porcine macrophage cell line PAM 3D4/31 is reported to rely on both glycolysis and OxPhos[59]. In agreement with primary alveolar macrophages[60], we show that the metabolic profile of the porcine macrophage cell line is of high

OxPhos/low anaerobic glycolysis metabolic fingerprint, indicated by the high activity of mitochondrial PDH-like enzymes and a lower contribution of cytosolic LDH-like enzymes. Mitochondria have been suggested to activate the ARTs inducing their mechanism of action[61,62] and that the drugs may interfere with the electron transport chain activity[63,64] potentially leading to ATP depletion and mitochondrial dysfunction[61,62]. Thus, using two-photon NAD(P)H-FLIM we detected drug induced reduction in their overall metabolic activity, dominated by high OxPhos, indicating an influence of the ARTs on the mitochondria.

Analysis of the energy and defense metabolism of the larvae using two-photon NAD(P)H-FLIM revealed two metabolically distinct regions within the larvae, i.e. the pharynx and the midgut. While both anatomical locations displayed similar metabolic profiles of energy production, oxidative burst attributed to NADPH-bound DUOX enzyme (DUOX-like enzymatic activity) was observed to a greater extent in the pharynx rather than in the midgut. Our data further revealed a higher overall metabolic activity within the pharynx region of the larvae when compared to that of the midgut. In mammalian cells, DUOX enzymes are mainly associated with defense metabolism via oxidative burst in phagocytic cells [65], however, they have also been linked to non-phagocytic neuronal cells[66]. Since the *A. suum* L3 (egg-stage) pharynx region is extensively filled with neuronal cell bodies[57], our finding could be indicative of a highly active nervous system. Defense metabolism due to DUOX oxidative burst against bacterial pathogens was reported mainly in the hypodermis and intestine of *C. elegans*[67] and predominantly high in the digestive system of *Heligmosomoides polygyrus*[18]. Therefore, NADPH-bound DUOX observed in our data, though mainly observed in the pharynx, could also indicate defense-related metabolism in *A. suum* larvae. Remarkably, DUOX activity has also been shown to be involved in cross-linking of tyrosine residues between collagens that are required for normal biogenesis and functioning of the cuticle in the model nematode *C. elegans*[68]. Since the pharynx is an ectodermal tissue covered with cuticle while the midgut is mesodermal without cuticle, one might speculate that higher DUOX activity in the pharynx might be involved in maintenance of cuticle function.

The *A. suum* L3 (egg-stage) midgut consists of seven cells that contain deposits of glycogen and lipids[57,69,70] signifying energy production via glycogenolysis or lipolysis, respectively. In contrast, we show mitochondrial energy metabolism within the midgut to be denoted by metabolically active PDH and IDH enzymes. The absence of bound HADH implied energy production via aerobic glycolysis rather than beta oxidation of fatty acids, a characteristic of lipolysis. We found the energy metabolism of the entire larvae to be mainly associated with aerobic pathways, characterized by the preferential activity of the mitochondrial enzymes PDH and IDH, as compared to low activity of LDH (associated with anaerobic glycolysis) and no activity of MDH. This was in agreement with aerobic respiration

required for larval development during their hepato-tracheal migration[32,33], ARTs, however, had no impact on NAD(P)H-bound enzymes related to bioenergetics (PDH and IDH) indicating no shift in the high OxPhos/low anaerobe glycolysis metabolic fingerprint. In addition, exposed larvae were observed to have an unperturbed NAD(P)H-dependent general metabolic activity.

Concluding, by adapting and applying two-photon NAD(P)H-FLIM to analyze overall metabolic activity and preferential enzymatic activities in porcine macrophages and in *A. suum* L3, we found dominantly mitochondrial energy metabolism in both host and parasitic larvae, characterized by high OxPhos/low anaerobe glycolysis. This dominant metabolic profile was not influenced by exposure to ARTs. The drugs effected only the overall metabolic activity of the host macrophages, but not on the parasite metabolism. Surprisingly, we found a high DUOX-like activity in the pharynx of the *A. suum* L3, which we attributed to a possible oxidative burst. Further functions related to DUOX-like activity in *A. suum* larvae need further investigation in future studies.

As the use of two-photon NAD(P)H-FLIM allows for resolution of changes in overall metabolic and specific enzymatic activities, we expect that the method retains the potential to improve our understanding of host-parasite metabolic crosstalk and, by that, of host-parasite interactions in general.

References

1. Lakowicz, J. R., Szmacinski, H., Nowaczyk, K. & Johnson, M. L. Fluorescence lifetime imaging of free and protein-bound NADH. *Proceedings of the National Academy of Sciences* **89**, 1271–1275 (1992).
2. Bird, D. K. *et al.* Metabolic mapping of MCF10A human breast cells via multiphoton fluorescence lifetime imaging of the coenzyme NADH. *Cancer Res* **65**, 8766–73 (2005).
3. Skala, M. C. *et al.* In vivo multiphoton fluorescence lifetime imaging of protein-bound and free nicotinamide adenine dinucleotide in normal and precancerous epithelia. *J Biomed Opt* **12**, 024014 (2007).
4. Mossakowski, A. A. *et al.* Tracking CNS and systemic sources of oxidative stress during the course of chronic neuroinflammation. *Acta Neuropathol* **130**, 799–814 (2015).
5. Radbruch, H. *et al.* Ongoing oxidative stress causes subclinical neuronal dysfunction in the recovery phase of EAE. *Front Immunol* **7**, (2016).
6. Barroso, M., Monaghan, M. G., Niesner, R. & Dmitriev, R. I. Probing organoid metabolism using fluorescence lifetime imaging microscopy (FLIM): The next frontier of drug discovery and disease understanding. *Adv Drug Deliv Rev* **201**, 115081 (2023).
7. Niesner, R., Peker, B., Schlüsche, P. & Gericke, K.-H. Noniterative biexponential fluorescence lifetime imaging in the investigation of cellular metabolism by means of NAD(P)H autofluorescence. *Chemphyschem* **5**, 1141–9 (2004).
8. Leben, R., Köhler, M., Radbruch, H., Hauser, A. E. & Niesner, R. A. Systematic Enzyme Mapping of Cellular Metabolism by Phasor-Analyzed Label-Free NAD(P)H Fluorescence Lifetime Imaging. *Int J Mol Sci* **20**, 5565 (2019).
9. Niesner, R. *et al.* Selective Detection of NADPH Oxidase in Polymorphonuclear Cells by Means of NAD(P)H-Based Fluorescence Lifetime Imaging. *Journal of Biophysics* **2008**, 1–13 (2008).

10. Blacker, T. S. & Duchen, M. R. Investigating mitochondrial redox state using NADH and NADPH autofluorescence. *Free Radic Biol Med* **100**, 53–65 (2016).
11. Stringari, C., Sierra, R., Donovan, P. J. & Gratton, E. Label-free separation of human embryonic stem cells and their differentiating progenies by phasor fluorescence lifetime microscopy. *J Biomed Opt* **17**, 046012 (2012).
12. Jumaa, H. *et al.* Immunoglobulin expression in the endoplasmic reticulum shapes the metabolic fitness of B lymphocytes. *Life Sci Alliance* **3**, (2020).
13. Leben, R. *et al.* Phasor-Based Endogenous NAD(P)H Fluorescence Lifetime Imaging Unravels Specific Enzymatic Activity of Neutrophil Granulocytes Preceding NETosis. *Int J Mol Sci* **19**, (2018).
14. Datta, R., Alfonso-Garciá, A., Cinco, R. & Gratton, E. Fluorescence lifetime imaging of endogenous biomarker of oxidative stress. *Sci Rep* **5**, (2015).
15. Neto, N. G. B. *et al.* Non-invasive classification of macrophage polarisation by 2P-FLIM and machine learning. *Elife* **11**, (2022).
16. Alfonso-García, A. *et al.* Label-free identification of macrophage phenotype by fluorescence lifetime imaging microscopy. *https://doi.org/10.1117/1.JBO.21.4.046005* **21**, 046005 (2016).
17. Bess, S. N., Igoe, M. J., Denison, A. C. & Muldoon, T. J. Autofluorescence imaging of endogenous metabolic cofactors in response to cytokine stimulation of classically activated macrophages. *Cancer & Metabolism 2023 11:1* **11**, 1–16 (2023).
18. Liublin, W. *et al.* NAD(P)H fluorescence lifetime imaging of live intestinal nematodes reveals metabolic crosstalk between parasite and host. *Sci Rep* **12**, 7264 (2022).
19. Elizalde-Velázquez, L. E. *et al.* Th2 and metabolic responses to nematodes are independent of prolonged host microbiota abrogation. *Parasite Immunol* **45**, e12957 (2023).
20. Stringari, C. *et al.* Multicolor two-photon imaging of endogenous fluorophores in living tissues by wavelength mixing. *Sci Rep* **7**, (2017).
21. Gallego-López, G. M., Guzman, E. C., Knoll, L. J. & Skala, M. Metabolic changes to host cells with Toxoplasma gondii infection. *bioRxiv* (2023) doi:10.1101/2023.08.10.552811.
22. Schlosser-Brandenburg, J. *et al.* Infection with soil-transmitted helminths and their impact on coinfections. *Frontiers in Parasitology* **2**, (2023).
23. Sartorius, B. *et al.* Prevalence and intensity of soil-transmitted helminth infections of children in sub-Saharan Africa, 2000–18: a geospatial analysis. *Lancet Glob Health* **9**, e52–e60 (2021).
24. Khanal, S., Maharjan, S. S., Aryal, D. & Acharya, S. P. Ascaris infestation leading to diarrhea and malnutrition. *Bangladesh Critical Care Journal* **5**, 70–71 (2017).
25. Abdellatif, M. Z. M., Belal, U. S., Abdel-Hafeez, E. H., Atiya, A. M. & Norose, K. Ascaris lumbricoides causing acute abdomen: a case report. *East Mediterr Health J* **19**, 1035–7 (2013).
26. Midha, A., Ebner, F., Schlosser-Brandenburg, J., Rausch, S. & Hartmann, S. Trilateral Relationship: Ascaris, Microbiota, and Host Cells. *Trends in Parasitology* Preprint at https://doi.org/10.1016/j.pt.2020.09.002 (2020).
27. Easton, A. *et al.* Molecular evidence of hybridization between pig and human ascaris indicates an interbred species complex infecting humans. *Elife* **9**, 1–26 (2020).
28. Mendes, Â. J., Ribeiro, A. I., Severo, M. & Niza-Ribeiro, J. A multilevel study of the environmental determinants of swine ascariasis in England. *Prev Vet Med* **148**, 10–20 (2017).
29. Coakley, G. *et al.* Immune serum-activated human macrophages coordinate with eosinophils to immobilize Ascaris suum larvae. *Parasite Immunol* **42**, (2020).
30. Wu, Y. *et al.* Transient Ascaris suum larval migration induces intractable chronic pulmonary disease and anemia in mice. *PLoS Negl Trop Dis* **15**, e0010050 (2021).
31. Holland, C. V. The long and winding road of Ascaris larval migration: the role of mouse models. *Parasitology* **148**, 1–9 (2021).
32. Takamiya, S. *et al.* Developmental changes in the respiratory chain of Ascaris mitochondria. *Biochimica et Biophysica Acta (BBA) - Bioenergetics* **1141**, 65–74 (1993).

33. Kita, K. Electron-transfer complexes of mitochondria in Ascaris suum. *Parasitology Today* **8**, 155–159 (1992).
34. Kita, K., Hirawake, H., Miyadera, H., Amino, H. & Takeo, S. Role of complex II in anaerobic respiration of the parasite mitochondria from Ascaris suum and Plasmodium falciparum. *Biochim Biophys Acta* **1553**, 123–39 (2002).
35. Tielens, A. G. Energy generation in parasitic helminths. *Parasitol Today* **10**, 346–52 (1994).
36. Liao, F. Discovery of Artemisinin (Qinghaosu). *Molecules* **14**, 5362–5366 (2009).
37. Ho, W. E., Peh, H. Y., Chan, T. K. & Wong, W. S. F. Artemisinins: Pharmacological actions beyond anti-malarial. *Pharmacol Ther* **142**, 126–139 (2014).
38. Meshnick, S. R. Artemisinin: Mechanisms of action, resistance and toxicity. in *International Journal for Parasitology* vol. 32 1655–1660 (Pergamon, 2002).
39. Qiu, N. *et al.* Artemisinin inhibits NRas palmitoylation by targeting the protein acyltransferase ZDHHC6. *Cell Chem Biol* **29**, 530-537.e7 (2022).
40. Makanga, M., Bray, P. G., Horrocks, P. & Ward, S. A. Towards a proteomic definition of CoArtem action in Plasmodium falciparum malaria. *Proteomics* **5**, 1849–58 (2005).
41. Ismail, H. M. *et al.* Artemisinin activity-based probes identify multiple molecular targets within the asexual stage of the malaria parasites Plasmodium falciparum 3D7. *Proc Natl Acad Sci U S A* **113**, 2080–5 (2016).
42. Shuhua, X., Hotez, P. J. & Tanner, M. Artemether, an effective new agent for chemoprophylaxis against shistosomiasis in China: its in vivo effect on the biochemical metabolism of the Asian schistosome. *Southeast Asian J Trop Med Public Health* **31**, 724–32 (2000).
43. Mi, Y. *et al.* Dihydroartemisinin Inhibits Glucose Uptake and Cooperates with Glycolysis Inhibitor to Induce Apoptosis in Non-Small Cell Lung Carcinoma Cells. *PLoS One* **10**, e0120426 (2015).
44. Jin, J. *et al.* Artesunate Inhibits the Development of Esophageal Cancer by Targeting HK1 to Reduce Glycolysis Levels in Areas With Zinc Deficiency. *Front Oncol* **12**, 871483 (2022).
45. Chen, L., Wang, C., Hu, N. & Zhao, H. Artesunate enhances adriamycin cytotoxicity by inhibiting glycolysis in adriamycin-resistant chronic myeloid leukemia K562/ADR cells. *RSC Adv* **9**, 1004–1014 (2019).
46. Xiao, F. *et al.* Artesunate suppresses Th17 response via inhibiting IRF4-mediated glycolysis and ameliorates Sjoğren's syndrome. *Signal Transduction and Targeted Therapy 2022 7:1* **7**, 1–3 (2022).
47. Zhou, Y. *et al.* In vitro efficacy of artemisinin-based treatments against SARS-CoV-2. *Sci Rep* **11**, 14571 (2021).
48. Midha, A. *et al.* The Intestinal Roundworm Ascaris suum Releases Antimicrobial Factors Which Interfere With Bacterial Growth and Biofilm Formation. *Front. Cell. Infect. Microbiol* **8**, 271 (2018).
49. Kundik, A. *et al.* Quantifying metabolic activity of Ascaris suum L3 using resazurin reduction. *Parasites & Vectors 2023 16:1* **16**, 1–13 (2023).
50. Urban, J. F. , Jr., Douvres, F. W. & Tromba, F. G. A rapid method for hatching Ascaris suum eggs in vitro. *Proc Helminthol Soc Wash* **48**, 241–243 (1981).
51. Jex, A. R. *et al.* Ascaris suum draft genome. *Nature* **479**, 529–533 (2011).
52. UniProt Consortium. UniProt: the Universal Protein Knowledgebase in 2023. *Nucleic Acids Res* **51**, D523–D531 (2023).
53. Paysan-Lafosse, T. *et al.* InterPro in 2022. *Nucleic Acids Res* **51**, D418–D427 (2023).
54. Digman, M. A., Caiolfa, V. R., Zamai, M. & Gratton, E. The phasor approach to fluorescence lifetime imaging analysis. *Biophys J* **94**, (2008).
55. Leben, R., Köhler, M., Radbruch, H., Hauser, A. E. & Niesner, R. A. Systematic Enzyme Mapping of Cellular Metabolism by Phasor-Analyzed Label-Free NAD(P)H Fluorescence Lifetime Imaging. *Int J Mol Sci* **20**, (2019).

56. Niesner, R. *et al.* Selective detection of NADPH oxidase in polymorphonuclear cells by means of NAD(P)H-based fluorescence lifetime imaging. *J Biophys* **2008**, 1–13 (2008).
57. Nichols, R. L. The Etiology of Visceral Larva Migrans: II. Comparative Larval Morphology of Ascaris lumbricoides, Necator americanus, Strongyloides stercoralis and Ancylostoma caninum. *J Parasitol* **42**, 363 (1956).
58. Arzt, M. *et al.* LABKIT: Labeling and Segmentation Toolkit for Big Image Data. *Front Comput Sci* **4**, 777728 (2022).
59. Jeon, E. H. *et al.* Glucose-6-phosphate transporter mediates macrophage proliferation and functions by regulating glycolysis and mitochondrial respiration. *Biochem Biophys Res Commun* **524**, 89–95 (2020).
60. Wculek, S. K., Dunphy, G., Heras-Murillo, I., Mastrangelo, A. & Sancho, D. Metabolism of tissue macrophages in homeostasis and pathology. *Cellular & Molecular Immunology 2021 19:3* **19**, 384–408 (2021).
61. De Sarkar, S. *et al.* The leishmanicidal activity of artemisinin is mediated by cleavage of the endoperoxide bridge and mitochondrial dysfunction. *Parasitology* **146**, 511–520 (2019).
62. Hou, H. *et al.* Effects and Mechanism of Action of Artemisinin on Mitochondria of Plasmodium berghei. *Chin J Integr Med* **26**, 277–282 (2020).
63. Wang, J. *et al.* Artemisinin directly targets malarial mitochondria through its specific mitochondrial activation. *PLoS One* **5**, e9582 (2010).
64. Kumar, S. P., Jasrai, Y. T., Pandya, H. A., George, L.-B. & Patel, S. K. Structural insights into the theoretical model of Plasmodium falciparum NADH dehydrogenase and its interaction with artemisinin and derivatives: towards global health therapeutics. *OMICS* **17**, 231–41 (2013).
65. Babior, B. M., Lambeth, J. D. & Nauseef, W. The Neutrophil NADPH Oxidase. *Arch Biochem Biophys* **397**, 342–344 (2002).
66. Damiano, S. *et al.* Reactive Oxygen Species Regulate the Levels of Dual Oxidase (Duox1-2) in Human Neuroblastoma Cells. *PLoS One* **7**, 34405 (2012).
67. Chávez, V., Mohri-Shiomi, A. & Garsin, D. A. Ce-Duox1/BLI-3 generates reactive oxygen species as a protective innate immune mechanism in Caenorhabditis elegans. *Infect Immun* **77**, 4983–4989 (2009).
68. Edens, W. A. *et al.* Tyrosine cross-linking of extracellular matrix is catalyzed by Duox, a multidomain oxidase/peroxidase with homology to the phagocyte oxidase subunit gp91phox. *J Cell Biol* **154**, 879–91 (2001).
69. Jenkins, D. C. & Erasmus, D. A. The ultrastructure of the intestine of Ascaris suum larvae. *Z Parasitenkd* **35**, 173–87 (1971).
70. Wang, T. *et al.* Quantitative lipidomic analysis of Ascaris suum. *PLoS Negl Trop Dis* **14**, e0008848 (2020).

Acknowledgments

The authors would like to thank Beate Anders, Yvonne Weber, Bettina Sonnenburg, Marion Müller, and Christiane Palissa for adult worm collection, methodological and technical support. We also thank Anne Winkler for illustrative support.

Author Contributions

Conceptualization: SH, PHS, SR, ZDM; Investigation: ZDM, RL, AK; Data curation: ZDM, RL; Formal analysis and Visualization: ZDM, RL; Data interpretation: ZDM, RL, JK, RN, SH; Supervision: SH, RN; Funding acquisition: SH, RN; Resources: SH, RN, AEH; Writing -original draft: ZDM, SH, RL; Writing – review & editing: ZDM, RL, AK, JK, AEH, SR, PHS, RN, SH. All authors have read and agreed to the published version of the manuscript.

Data availability

All data that support the findings of this study are included within this paper and its FLIM image files are available from the corresponding author upon request.

Funding

This research was supported by German Research Foundation within the priority program 2332 "Physics of Parasitism" to SH, RN, SR, AEH [grant numbers HA2542/12-1, NI1167/7-1, RA2544/1-1, HA 5354/11-1] and GRK 2046/2-2019 to SH and SR as well as HA 2542/11-1 to SH. ZDM was supported by the German Academic Exchange Service (DAAD) [Grant reference 57507871]. PHS thanks the Max-Planck Society for generous financial support.

Competing interests

The authors declare no competing interests.